CHALMERS

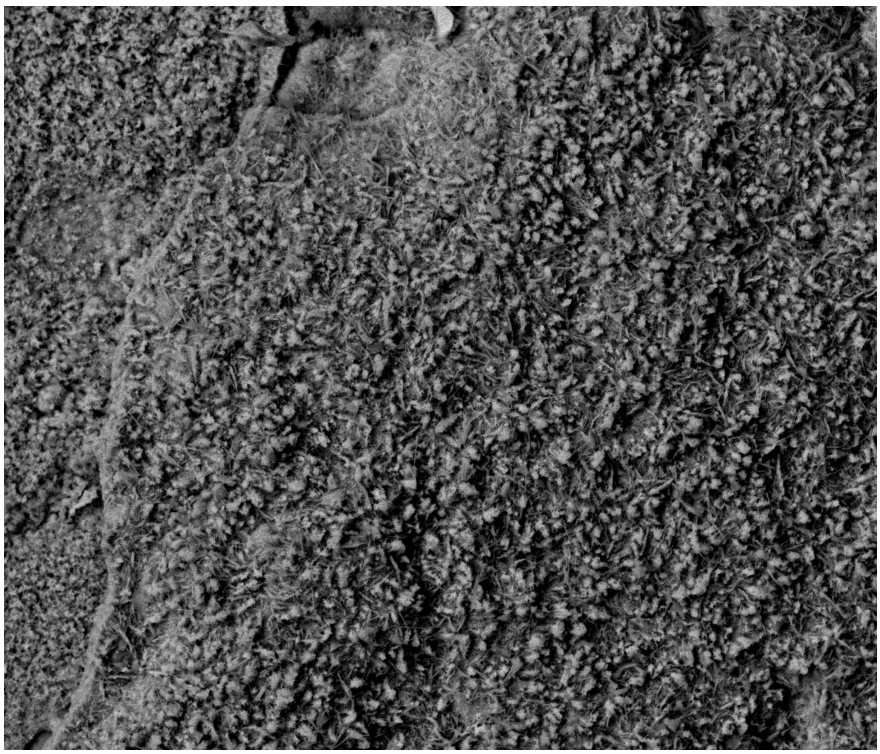

Corrosion Assessment of Materials for a Chemical Looping Combustion Air Reactor Used for Carbon Capture and Storage

Bachelor's degree project report in Chemical Engineering

Mohammad Ataia
David Fuhrman

Department of Chemistry and Chemical Engineering

CHALMERS UNIVERSITY OF TECHNOLOGY
Göteborg, Sweden 2025
www.chalmers.se

Corrosion Assessment of Materials for a Chemical Looping Combustion Air Reactor Used for Carbon Capture and Storage

Mohammad Ataia
David Fuhrman

CHALMERS

Department of Chemistry and Chemical Engineering
Division of Energy and Materials
CHALMERS UNIVERITY of TECHNOLOGY
Gothenburg, Sweden 2025

Corrosion Assessment of Materials for a Chemical Looping Combustion Air Reactor Used for Carbon Capture and Storage

Supervisor: Hooman Karimi Abadeh, Division of Energy and Materials, Chalmers University of Technology

Examiner: Jesper Liske, Division of Energy and Materials, Chalmers University of Technology

Cover: Image of oxide formation from a AISI 347H sample exposed to a clean environment at 600 °C for 168 h. The image is taken with an SEM instrument and has a magnification of 1000x.

Bachelor's Thesis 2025
Department of Chemistry and Chemical Engineering
Chalmers University of Technology
SE-41296 Göteborg
Tel: +46 31 772 10 00

Table of Contents

Abstract

Chemical Looping Combustion (CLC) with Carbon Capture and Storage (CCS) has shown promising advancements regarding carbon negative emissions. To increase the electrical efficiency of CLC, optimized corrosion resistance of the superheaters is crucial. This study focused on the air reactor (AR) of the CLC system at 600 °C and its potential corrosion hot spots at the superheaters. Six different alloys were tested in a clean and an alkali slip (0.5 ppm KOH) laboratory environment. Through gravimetric measurements and scanning electron microscope micrographs, the results showed that the Ni-based alloys and the ferritic FeCrAl alloys performed best from a corrosion point of view. Ferritic steels and austenitic stainless steels, strengthened the issue by showing poorer gravimetric and micrographic results.

Nomenclature

AR – Air Reactor

BECCS – Bioenergy with Carbon Capture and Storage

CCS – Carbon Capture and Storage

CLC – Chemical Looping Combustion

CO_2 – Carbon Dioxide

CO_x – Carbon Oxide

FR – Fuel Reactor

H_2O - Water

HCl – Hydrochloride

K_2CO_3 - Potassium Carbonate

KCl – Potassium Chloride

Me_xO_y – Oxidized state of Oxygen Carrier

Me_xO_{y-1} – Reduced state of Oxygen Carrier

NaCl – Sodium Chloride

NO_x – Nitrogen Oxide

OC – Oxygen Carrier

SEM-EDX – Scanning Electron Microscopy with Energy Dispersive X-ray

SO_x – Sulfur Oxide

Acknowledgements

We would first and foremost like to thank our supervisor Hooman Karimi Abadeh and our examiner Jesper Liske for their guidance and encouragement in our work. Their constant support and tips throughout this process, both in the lab and during the writing process, has helped us massively. We would also like to extend our thanks to friends and family who have supported us through this process.

1. Introduction

The world faces a significant challenge today as the average global temperature steadily increases[1]. With over 70% of today's heat and power production derived from fossil fuel combustion, this is possibly linked to the problem at hand. Depending on whether the world's attitude toward combating this issue and focus more on renewable energy sources changes, the problem can be expected to grow over the next few decades. CO_2 is the most prominent greenhouse gas in the atmosphere today and the main source of CO_2 emission continues to be fossil fuel combustion. Therefore, reducing both the existing pollution and the origin of CO_2 is of vital importance to ensure a positive change for the climate[2].

During fossil fuel combustion, several harmful emissions are released, namely CO_x, NO_x and SO_x. Due to the nature of hydrocarbons, the combustion of coal, oil and natural gases mainly releases CO_2 into the atmosphere. CO_2 is particularly harmful due to its long atmospheric lifetime causing a cumulative effect on global warming[2].

This increase in fossil fuel consumption has led to innovative solutions to combat the problem. The most obvious is the development of green energy alternatives such as solar, wind and biomass heat and power generation. These alternatives are a step in the right direction since they are ideally carbon neutral. However, in today's climate, more drastic measures are needed to mitigate the carbon emissions. Therefore, Carbon Capture and Storage (CCS) has been explored as it has the potential to be carbon negative. CCS's addition to bio energy power plants can result in an effectively negative carbon emission since biomass is considered a carbon neutral fuel[2].

Bioenergy with Carbon Capture and Storage (BECCS) is a prominent technique in the so-called post-combustion method. Although oxy-fuel combustion is sometimes considered conceptually related to CLC, this study does not focus on it or on pre-combustion methods, as they are less relevant for the corrosion comparison with the CLC air reactor. Instead, the discussion is limited to post-combustion capture, which serves as a more practical point of reference. As the name suggests, in the post-combustion technology, CO_2 is handled after the combustion of the fuel. This results in a technology that can be retrofitted to an already existing power plant [3].

In the post-combustion method, chemical adsorption is used to capture the CO_2. Several methods of capturing the CO_2 have been applied in the past, there-among, amine-based solutions and aqueous ammonia. In recent years, aqueous ammonia has been shown to be a promising technology, which is still in development. An ammonia-based solution is used to selectively capture CO_2 from the flue gases created in the reactor[4].

The ammonia method has been shown to have several advantages over the other methods used. Compared to amine-based systems, aqueous ammonia offers lower heat of reaction, which in turn results in energy savings. However, the apparent downside of this process is the cooling of the flue gases needed to improve the adsorption of CO_2[2]. The amine-based method separates CO_2 with the help of a washing solution. Since this process operates at 120 – 140 °C, the energy penalty is lower than that of the aqueous ammonia. Many amines have been investigated to use as washing solution with Monoethanolamide (MEA) being applied in modern carbon capture plants[5].

However, the ammonia process does reduce the energy efficiency by 25-30%[6]. This, in addition to the potentially harmful environmental impacts of the washing solutions, contribute to a hesitance of industry in adopting this method. Moreover, building the infrastructure, retrofitting, and implementation of these systems is costly. In addition, the operating expenditures are higher for these systems compared to existing units. The significant energy demand of the post-combustion CO_2 capture and the need for continuous operation of the plant, compression and regeneration process, reduce the efficiency and potential profitability of the plant[5 7].

While the post-combustion method is the most prominent of the three mentioned, CLC offers lower energy requirements for CO_2 separation while also potentially enabling higher electrical efficiency during the combustion of biomass. Even though no commercial CLC units exist yet, small-scale units have been shown to be successful. This demonstrates the possibility to expand and amplify these units to reach commercial size[8].

Chemical looping combustion was first presented around 1950 by Lewis and Gilliland and has since then, constantly developed. It is now seen as a candidate for a CO_2 neutral combustion process[2]. Chemical looping combustion operates on the principle of spatially

separating the oxidation of fuel from the regeneration of the oxidizing agent, accomplished through the cyclical use of solid oxygen carrier materials[9] [10].

The process avoids direct contact between fuel and combustion air by employing a metal oxide oxygen carrier that transfers oxygen from air to fuel in a controlled manner[10]. This separation enables the production of a concentrated CO_2 stream without the need for energy-consuming gas separation processes that characterize conventional carbon capture approaches[10].

The CLC system consists of two interconnected fluidized bed reactors: a fuel reactor and an air reactor[9] [10]. In the fuel reactor, the fuel reacts with the oxygen carriers (OC), which supplies the necessary oxygen for combustion while simultaneously being reduced from its oxidized state[9]. The combustion products from this reaction consists primarily of CO_2 and water vapor, creating a concentrated CO_2 stream that can be purified through simple condensation of water vapor[10].

Meanwhile, the reduced OCs are transported to the air reactor, where they are regenerated through contact with air, releasing heat in the process[9]. The regenerated OCs are then returned to the fuel reactor, completing the cycle that defines the CLC process. The total heat released from both the reduction and oxidation reactions equal that of conventional combustion, ensuring that the overall energy balance remains unchanged[10].

However, the spatial separation of these reactions provides the advantage of producing separate gas streams: a concentrated CO_2 stream from the fuel reactor and a nitrogen-rich stream from the air reactor[9].

Many metal oxides have been tested as potential OC's; however, iron-based compounds have shown to be favourable due to its good thermodynamic properties in regard to the conversion to CO_2 and H_2O. Primarily, iron-, ilmenite- or manganese ores and iron-based waste are used in the interest of economic viability[11].

This systemic design recognises a combustion reactor which functions without the inflow of additional air, resulting in less flue gases disturbing the combustion in the FR.

It is suggested that this technology can reduce the energy penalty linked to gas separation by 50%, compared to conventional methods[8].

Chemical looping combustion has also shown a significant potential for increased power production compared to conventional heat and power plants using biofuels. During combustion, flue gases containing different alkalis, such as KCl, NaCl, K_2CO_3, HCl as well as water vapor, lead to severe corrosion during their interaction with the superheaters of the power plants. The accepted solution to this problem is a lower temperature in the conventional boilers' superheaters to mitigate the corrosion. In turn, a lower electrical efficiency is achieved throughout the system. With CLC, this issue is partly resolved thanks to the nature of its configuration. Since the heat extractions and electrical generation are located in different sections of the system, and with the superheaters located in the AR and distant from any fuel, the risk for corrosion is substantially lowered. Even though no alkali compounds are expected to travel to the AR, studies have revealed that small amounts of volatile alkali compounds could be transferred from the FR[8].

Biofuels are renewable fuels produced from biomass, which provide a sustainable substitute for fossil fuels. Their application is capable of lowering net greenhouse gas emissions, furthermore, they bring about energy security through lowering dependency on foreign fossil fuels. They are mainly utilized within transport, e.g., bioethanol and biodiesel for vehicles, but are finding new uses in aviation, electricity production, and domestic heating systems[12].

Because of the relatively low operating temperature in the conventional biomass reactor, low-melting compounds, such as alkali metal chlorides and sulphates, are carried over with the flue gases throughout the biomass reactors. These particles alongside the corrosive gases, HCl and Cl_2, released by the ongoing combustion, cause severe corrosion in the biomass reactors. In addition, the layers formed from the corrosion hinder heat transfer to the steam in the tubes[13].

The alloys investigated in this thesis are based on those of H. Lindmark's study, except for AISI 310H which was exchanged with P91. The six alloys allow for a comprehensive understanding of how they react to a corrosive environment. The materials can be classed according to austenitic stainless steel, Ni-based alloy and ferritic FeCrAl alloy. In table 1,

the different compositions of each metal are displayed. The tests were performed at 600 °C to investigate corrosion at a representative operating temperature. The exposure time of 168 h was chosen to study the initial corrosion since the understanding of its effect is imperative to understand corrosion in its later stages. Due to the potential alkali-slip between the CLC reactors, two different scenarios were recreated in the test setup. One clean scenario without alkali-slip (5% O_2 + 3% H_2O + N_2 bal.) and one scenario with alkali-slip (5% O_2 + 3% H_2O + N_2 bal. + 0.5 ppm KOH). In both scenarios, 5% O_2 is present to simulate the oxygen-depleted air that is expected to leave the AR and 3% H_2O to simulate the humidity expected in the AR[8].

1.2 Aim

The aim of this study is to assess the corrosivity of different metals possibly used in a chemical looping combustion air reactor by simulating an environment with the help of customized tube furnaces.

2. Materials and methods

2.1 Materials

The materials investigated in the present study are according to Table 1. The nominal compositions (wt.%) are presented in Table 1. [8]

Table 1: The chemical composition of investigated alloys

Alloy/Element (wt.%)	Fe	Cr	Al	Ni	Mo	Si	Mn	Co	Cu	W	Nb	Minor elements
P 91 (9Cr1MoV)	bal.	9.5	×	×	1.05	0.5	0.6	×	×	×	0.1	C, V
AISI 347H	bal.	17.5	×	11	×	1.8	×	×	×	×	0.7	C, Si
Sanicro® 25	bal.	22.5	×	25	×	0.5	1.5	3	3.6	0.5	×	C, N, P, S
Sanicro® 60	4	21.5	×	bal.	8.7	×	×	×	×	×	3.5	C, P, S, Si, Mn
Sanicro® 63	11.1	22.1	×	bal.	4	×	×	×	×	×	×	C, N, Al, Si, Ti, Mn
Kanthal® EF101	bal.	12.4	4	×	×	1.3	×	×	×	×	×	C, Mn, RE*

2.2 Method

Prior to exposure, the edges of the samples were ground using 1000-grit paper and water as a lubricant until a uniform finish was achieved. Subsequently, the sample surfaces were further ground and polished through a sequence of progressively finer grit sizes. Eight samples were then placed in an automatic grinding machine using double-sided tape, grinding one side at a time. After each grinding cycle, the samples were cleaned with pressurized air, wiped with acetone and lint-less tissues. The process was repeated up to 4000-grit SiC papers, then a polishing cloth was used to further smooth the surface of the specimen to 3 and 1 µm. Finally, the samples were placed in acetone-filled containers subjected to ultrasonic agitation for 25 minutes. The samples were later stored in a desiccator.

Before exposure, the samples were weighed using high-precision SartoriousTM scales capable of microgram resolution. This step was repeated three times per sample, and the

average was recorded. The dimensions of the samples were then measured using a digital caliper on each of the four sides and along the depth, since the sample length could vary slightly due to overgrinding.

Following sample preparation, the tube furnaces were calibrated to the target exposure temperature necessary for the corrosion experiments. The test temperature of 600 ℃ was selected and applied on all samples.

Although the intended exposure temperature for the sample was set to 600 °C, the furnaces were deliberately set to 620 °C, which is slightly above the desired exposure temperature. The adjustment was made to compensate for temperature discrepancies arising within the system.

Once the tube furnace reached the set temperature, the distance between the tube and the furnace body was measured. A thermometer was marked from 0 to 70 cm in one-centimeter intervals, starting from the tube's entrance. It was mounted and centered inside the tube, then inserted one centimeter at a time and held in each position for two minutes, or until the temperature stabilized. The observed temperature was recorded in a spreadsheet. This procedure was repeated for all 70 positions or until the end of the furnace was reached. After the hotspot was identified, the furnace's set temperature was adjusted accordingly to match the target temperature, based on the deviation observed. The rod was then reinserted into the furnace starting from the hotspot, advancing one centimeter at a time to confirm that the temperature did not increase again within five centimeters of the new starting point.

The samples were carefully placed in sample holders made of Alumina (Al_2O_3). Each holder had three distinct slots in which the samples were positioned upright. If a sample did not fit due to overgrinding, a small piece of gold (Au) was inserted between the slot and the sample to ensure stability during exposure. The sample holder was placed on a sheet of paper, indicating the position of each metal and marking the airflow direction.

A sample holder contains the test alloys were placed in the furnaces' hotspots. A humidifier was activated to introduce water vapor into the system. Following this, the sample holder was inserted into the tube furnace using a metal rod, ensuring placement

within the hotspot region using length markers. Once all components were in position, the tube furnace was sealed. A two-way valve connected to distilled water is installed to monitor system integrity as any leakage would disrupt the formation of bubbles, which otherwise indicated an airtight setup. To further minimize potential thermal leaks, heating cords covered by aluminum foil were wrapped around all joints and access points. With these conditions established, the exposure timer was initiated.

After exposure for 168 hours (1 week), the sample holder was extracted and allowed to cool (to reduce burn risk) in a desiccator. The samples were then removed from their holders and weighed using the same method as before.

After weighing, the samples are sectioned and mounted for metallographic analysis. Surface morphology and oxide structures are examined by scanning electron microscopy (SEM), and elemental distribution is assessed through energy dispersive X-ray (EDX).

3. Analysis method

3.1 Scanning Electron Microscopy (SEM-EDX)

To analyse the samples after exposure, scanning electron microscopy (SEM) of the model FEI QUANTA ESEM 200 operated in high vacuum mode was used. SEM plan view micrographs were taken while using backscattering electrons (BSE) and secondary electrons (SE) at an accelerated electron voltage ranging between 12.5 – 20 keV.

4. Results

4.1 Weight gain

4.1.1 Clean Scenario

In Table 1, the average weight gain of each sample is shown. The most notable increase is that of P91, with its 2.37 mg/cm^2.
Concerning stainless steels, AISI 347H showed a significant increase in its clean scenario with a weight increase of 0.85 mg/cm^2 compared to Sanicro 25 which had an average weight gain of only 0.029 mg/cm^2.
Regarding the Ni-based alloys, Sanicro 60's average weight gain in the clean environment was especially low with a 0.0062 mg/cm^2 increase as opposed to the 0.019 mg/cm^2 of Sanicro 63.
EF101 showed an average weight gain of 0.017 mg/cm^2.

4.1.2 Alkali Slip Scenario

Table 2 also notes the average weight gain of the samples in the alkali slip (KOH) environment. The most notable weight gain can be seen for P91 again, with 5.16 mg/cm^2 in the alkali slip scenario. This shows that P91 had the highest average weight gain across both scenarios. In the alkali slip scenario, the stainless steels showed almost opposite results to the clean scenario with AISI 347H gaining an average of 0.064 mg/cm^2 while Sanicro 25 showed an average weight gain of 0.101 mg/cm^2. The low weight gain of AISI 347H is attributed to the spallation of the oxide scale which was seen when the samples were cooling. In the matter of Ni-based alloys, both Sanicro 60 and Sanicro 63 showed an average weight gain of 0.079 and 0.056 mg/cm^2 respectively. In the alkali slip environment, EF101 showed the lowest average weight gain of 0.044 mg/cm^2 among all the samples.

Table 2: Overview of the average weight gain of each metal in both the clean and alkali slip (KOH) scenario

Sample	Pre-exposure weight avg.	Post-exposure weight avg.	Surface area (cm^2)	Weight gain (mg/cm^2)
EF101 (clean)	1.650418	1.650477	3.705232	0.016013
San 60 (clean)	2.076208	2.076231	3.726046	0.006173
San 63 (clean)	1.940513	1.940584	3.659436	0.019311
San 25 (clean)	1.609792	1.609887	3.251814	0.029184
347H (clean)	1.790419	1.793399	3.501888	0.851065
P91 (clean)	3.096739	3.109649	5.452921	2.367538
EF101 (KOH)	1.751536	1.751697	3.693688	0.043813
San 60 (KOH)	2.146352	2.14665	3.777126	0.078896
San 63 (KOH)	1.73866	1.738844	3.249531	0.056418
San 25 (KOH)	1.459483	1.459794	3.049656	0.101979
347H (KOH)	1.780822	1.781052	3.584204	0.06417
P91 (KOH)	3.006501	3.034404	5.41036	5.157266

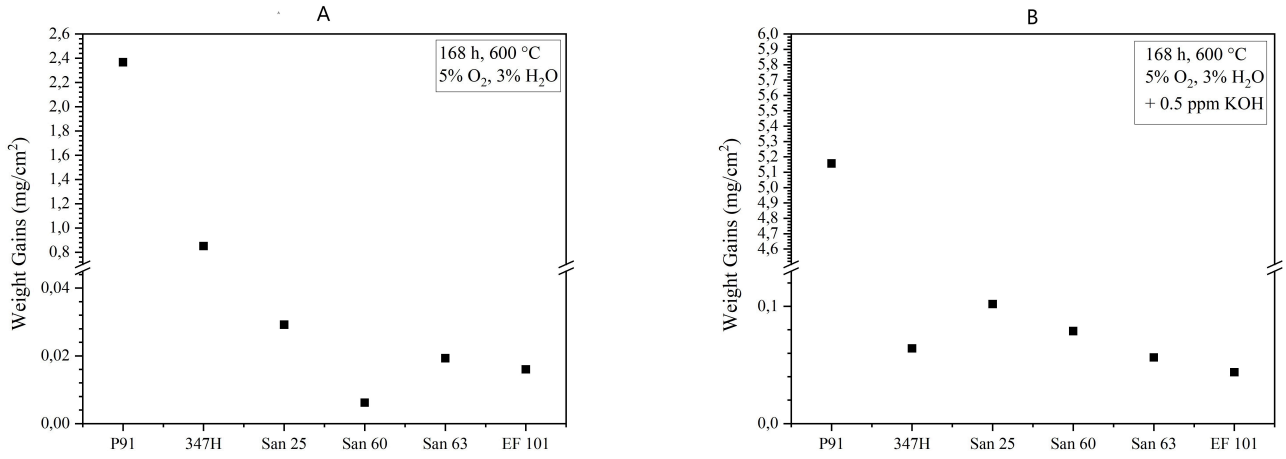

Figure 1: Average weight gain in clean (A) and alkali-slip (B) scenarios

4.2 Microstructural analysis in Clean scenario

4.2.1 500x magnification

4.2.1.1 P91 at 500x magnification

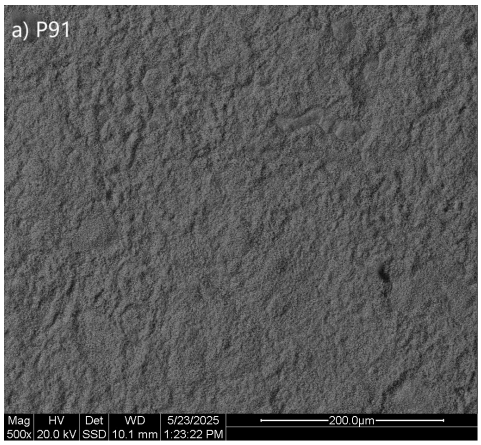

Figure 2: P91 at 500x magnification

The P91 sample (Figure 2) showed a homogenously corroded surface in the plan view SEM micrograph. As presented by Phother-Simon et al. [14], it is argued that the top layer is Hematite (Fe_2O_3) with a subsidiary layer of Magnetite (Fe_3O_4).

4.2.1.2 Stainless steels at 500x magnification

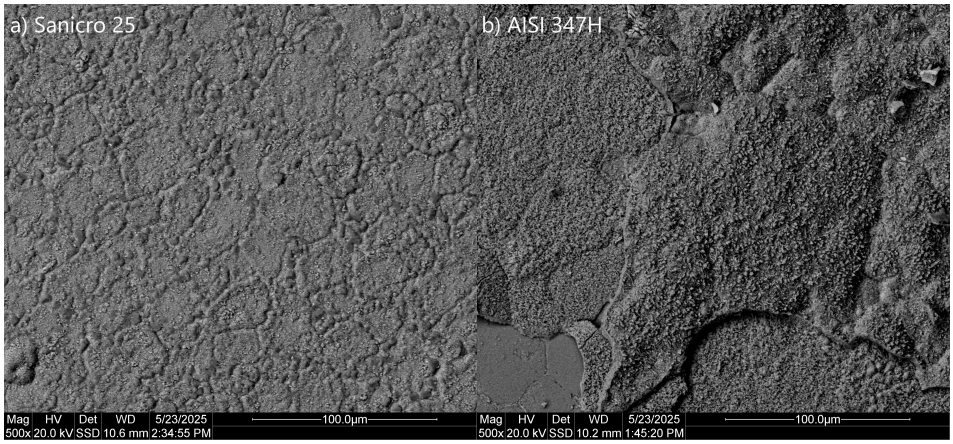

Figure 3: Stainless Steels at 500x magnification, a) Sanicro 25 b) AISI 347H

In Figure 3a, corrosion is seen to originate from the middle of the grains of Sanicro 25. A homogeneous corrosive layer has formed, appearing rich in iron and oxygen, which is consistent with the presence of iron oxides.

The SEM micrograph (figure 3b) of AISI 347H shows severe corrosion. Severe cracks and spallation are seen all over the surface of this sample. A spalled area can be seen on the left bottom side of the SEM micrographs. Here, the oxidation formed coincides with that of Sanicro 25.

4.2.1.3 Ni-based alloys at 500x magnification

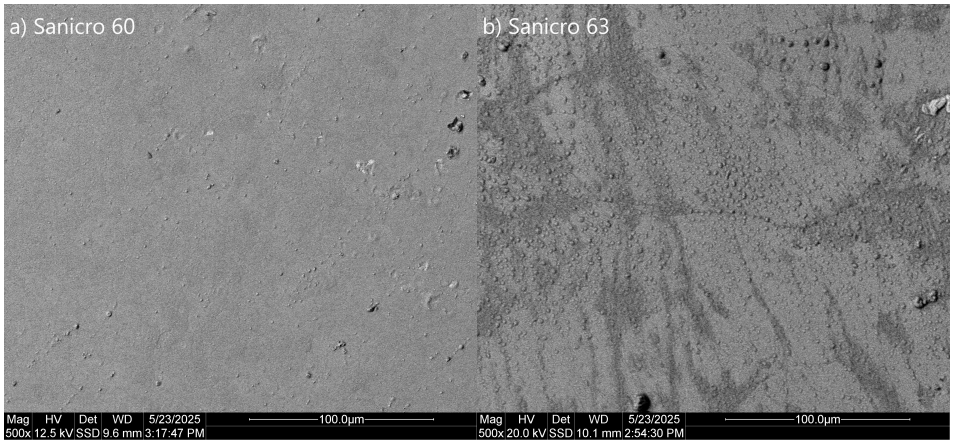

Figure 4: Ni-based alloys at 500x magnification, a) Sanicro 60 b) Sanicro 63

Sanicro 60 (Figure 4a) showed little to no corrosion in the SEM micrograph. The small nodules visible seem to be the only proof of corrosion in this case. However, from visual confirmation, a thin homogenous layer of oxidation can be confirmed due to blackening of the sample.

Figure 4b shows a homogenously corroded surface of Sanicro 63. This thin layer consists of nodules. The thin oxide scale allowed for the grains and grain boundaries to appear. Unlike the stainless steels, the corrosion does not form in the grain boundaries.

4.2.2 2000x – 5000x magnification

4.2.2.1 P91 at 5000x magnification

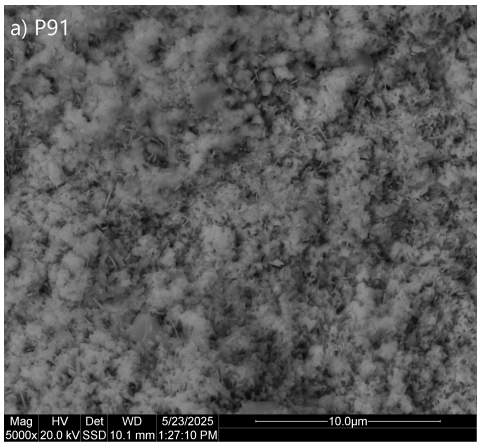

Figure 5: P91 at 5000x magnification

The abundant corrosion can now be identified with the increased magnification in Figure 5. A background of nodules with needles on top of them have been seen in this SEM micrograph. The needles are generally accepted as Hematite according to Lindmark et al. [15]. Moreover, EDX analysis showed an iron oxide surface layer with 40 atomic % Fe and 60 atomic % O, consistent with hematite formation.

4.2.2.2 Stainless steels at 2000x magnification

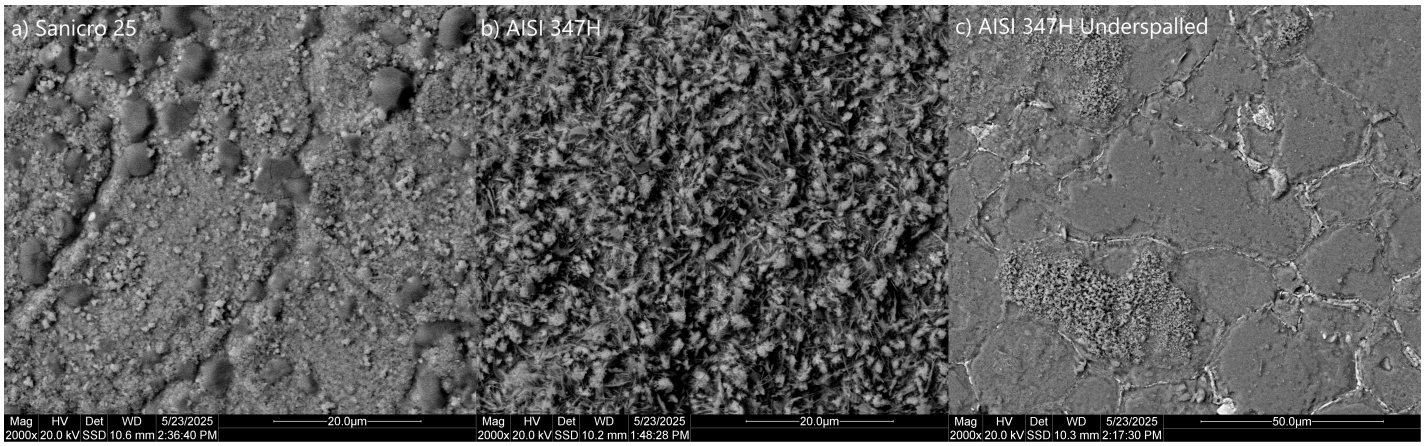

Figure 6: Stainless Steels at 2000x magnification, a) Sanicro 25 b) AISI 347H Overspalled c) AISI 347H Underspalled

With a higher magnification at Sanicro 25 in Figure 6a, the corrosion can now be seen to originate from the middle of the grains where corrosion is most severe. Again, EDX shows an iron rich oxide of 40 atomic % Fe and 60 atomic % O.

From the higher magnification image of AISI 347H (Figure 6b), bright needles of corrosion can be seen on the darker nodules, suggesting the presence of hematite. The regions with spallation show the same iron oxide in the EDX analysis.

In the regions without spallation of AISI 347H (Figure 6c), EDX indicates Fe-Cr rich oxides originate from the grain's centers. The brighter regions around the grains are interpreted as metallic nickel, since elements with higher atomic numbers, such as nickel, appear brighter in BSE imaging.

4.2.2.3 Ni-based alloys at higher magnification

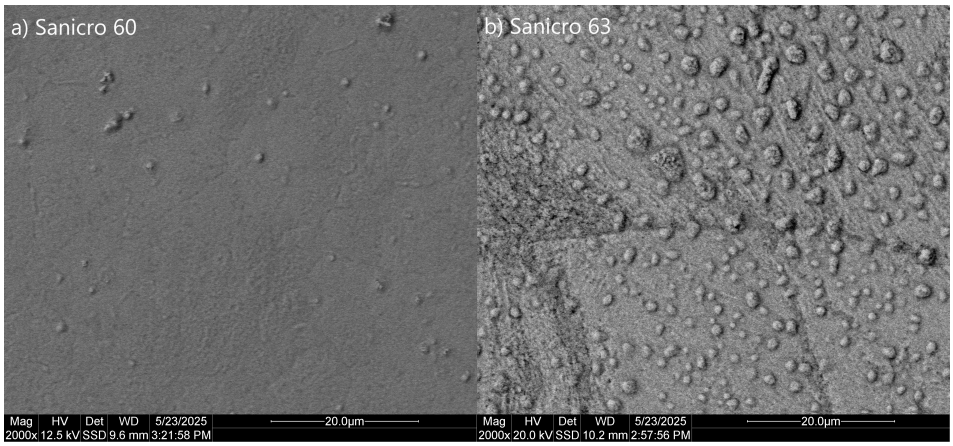

Figure 7: Ni-based alloys at 2000x magnification a) Sanicro 60 b) Sanicro 63

Even with the grain boundaries visible in Figure 7a, almost no indication of corrosion is visible from this SEM micrograph. The small amounts of oxidation formed are mostly a Cr-Ni oxide, shown by EDX. Since this alloy is a chromium former, the presence of Ni in the EDX results might be due to alloy itself. The analysis depth of the EDX is greater than the oxide thickness and signal from the underlying alloy is seen.

Figure 7b shows the homogeneity of Sanicro 63's corroded surface on a more detailed level. However, EDX could not distinguish between the nodules and original surface of the sample and showed a Fe-Cr-Ni rich oxide throughout the sample. According to Lindmark et al. [8] the most prominent chromium oxide to form is Cr_2O_3.

5. Discussion

The corrosion behavior of the investigated alloys highlights the role of chemical composition in determining high-temperature performance. Sanicro 25 and AISI 347H, although both stainless steels, exhibited different results. The superior corrosion resistance of Sanicro 25 can be linked to its higher nickel and chromium content, elements known to stabilize protective oxide scales, particularly Cr_2O_3. In contrast, P91, which contains no nickel and only a modest chromium level, performed the worst among all alloys, underscoring the importance of these elements in forming stable protective layers.

Interestingly, EF101 excelled despite containing no nickel. Its strong performance can be explained by its high chromium content combined with aluminum additions, which compensate for the absence of nickel by promoting the formation of protective alumina and chromia layers. Although no micrographs were obtained for EF101, its low weight gain places it on par with the Ni-based alloys and Sanicro 25. Overall, these findings emphasize the advantages of chromium and nickel in stainless steels, while also showing that aluminum can effectively substitute nickel in alloys such as EF101.

To ensure that the corrosion exposures reflected realistic operational conditions, the experiments were performed at 600 °C, a temperature representative of biomass reactors where alkali induced corrosion is a common degradation mechanism. The furnaces were deliberately set above this nominal value to account for thermocouple drift and heat losses caused by flowing gases, ensuring that the sample surface remained close to the intended temperature. Prior temperature mapping also identified the furnace hotspot, allowing for reliable control of exposure conditions throughout the test duration.

When comparing the clean and alkali-slip scenarios, the presence of KOH had a pronounced effect. For the Ni-based alloys and EF101, weight gain increased by a factor of 3–10 under alkali-slip conditions. Sanicro 25 showed a similar trend, whereas AISI 347H behaved differently: its clean exposures resulted in a 13-fold higher weight gain compared to alkali slip, which is explained by oxide scale spallation. Although P91 exhibited the highest absolute weight gain overall, the difference between its two scenarios was limited

to roughly a factor of two. Compared to data reported by Lindmark et al. [7] at 700 °C, the lower relative increases observed here confirm the robustness of the test system at 600 °C.

6. Conclusions

In conclusion, nickel and chromium have shown a crucial position in corrosion resistance in metals. The high performance in both gravimetrical tests and in SEM micrographs for Ni-based alloys implies that both nickel and chromium is a key contributor for strengthening corrosion resistance. The verification of poor corrosion resistance in P91, which isn't comprised of nickel and has a lower volume of chromium, again proves that both these metals are favorable contributors for improving corrosion resistance in metals.

In addition, outstanding performances achieved by EF101 in nickel free conditions demonstrate that alternative alloying strategies, for instance, addition of aluminum in conjunction with chromium, can reproduce the protective behaviors typically encountered in Ni-based alloys. The low weight gain experienced by EF101, which is at a level with Ni-based alloys, demonstrates that aluminum can replace nickel in developing a protective and favorable oxide scale, thus enabling a viable path towards designing high performance, nickel free corrosion resistant steels.

Overall, these findings suggest that several compositions of both nickel and chromium are advantageous while developing good corrosion resistant alloys. Despite the excellent result combining these two metals, EF101 identifies successful corrosion resistance combining chromium with aluminum. This creates further possibilities for designing alloys, in cases where lower use of nickel is preferred for economy or resources.

7. References

[1] T. M. Thiedemann and M. Wark, "A Compact Review of Current Technologies for Carbon Capture as Well as Storing and Utilizing the Captured CO2," *Processes,* vol. 13, no. 1, p. 283, 2025. [Online]. Available: https://www.mdpi.com/2227-9717/13/1/283.

[2] H. A. Alalwan and A. H. Alminshid, "CO2 capturing methods: Chemical looping combustion (CLC) as a promising technique," *Sci Total Environ,* vol. 788, p. 147850, 2021/09/20/ 2021, doi: https://doi.org/10.1016/j.scitotenv.2021.147850.

[3] J. Inumaru, T. Hasegawa, H. Shirai, H. Nishida, N. Noda, and S. Ohyama, "Fossil fuels combustion and environmental issues," 2021, pp. 1-56.

[4] L. Petrescu, D. Bonalumi, G. Valenti, A.-M. Cormos, and C.-C. Cormos, "Life Cycle Assessment for supercritical pulverized coal power plants with post-combustion carbon capture and storage," *J Clean Prod,* vol. 157, pp. 10-21, 2017/07/20/ 2017, doi: https://doi.org/10.1016/j.jclepro.2017.03.225.

[5] D. Möller, "Chemistry for Environmental Scientists (2nd Edition)," De Gruyter.

[6] H. Yu, L. Li, M. Maeder, K. Li, and M. Tade, *Process Modelling of Combined SO_2 and CO_2 Capture Using Aqueous Ammonia*. Newcastle, Australia: CSIRO Energy Technology, 2008. [Online].Available: https://www.globalccsinstitute.com/archive/hub/publications/198523/process-modelling-combined-so2-co2-capture-using-aqueous-ammonia.pdf

[7] Q. Wang, "Post-Combustion Carbon Dioxide Capture Materials," Royal Society of Chemistry (RSC).

[8] H. Lindmark, R. Faust, T. Sand, L.-G. Johansson, P. Knutsson, and J. Liske, "Corrosivity of KOH(g) towards superheater materials in a simulated air reactor environment for chemical looping combustion of biomass," *Fuel,* vol. 381, p. 133178, 2025/02/01/ 2025, doi: https://doi.org/10.1016/j.fuel.2024.133178.

[9] U.S. Department of Energy, National Energy Technology Laboratory, “Chemical Looping Combustion,” NETL, 2022. [Online]. Available: https://www.netl.doe.gov/node/7478. [Accessed: Jul. 29, 2025]

[10] A. Lyngfelt, “CO_2 Chemical-Looping Combustion,” Chalmers University of Technology, Göteborg, Sweden. [Online]. Available: https://www.entek.chalmers.se/~anly/co2/CO2CLC.htm. [Accessed: Jul. 29, 2025]

[11] B. Fleiß, J. Priscak, M. Hammerschmid, J. Fuchs, S. Müller, and H. Hofbauer, "CO2 capture costs of chemical looping combustion of biomass: A comparison of natural and synthetic oxygen carrier," *Journal of Energy Chemistry,* vol. 92, pp. 296-310, 2024/05/01/ 2024, doi: https://doi.org/10.1016/j.jechem.2024.01.048.

[12] "Introduction," in *Biofuels: Securing the Planet’s Future Energy Needs*, A. Demirbas Ed. London: Springer London, 2009, pp. 1-44.

[13] W. B. A. (Sandy) Sharp, “Superheater Corrosion in Biomass Boilers: Today’s Science and Technology,” ORNL/TM-2011/399, Oak Ridge National Laboratory, Oak Ridge, TN, Sept. 30, 2010. [Online]. Available: https://info.ornl.gov/sites/publications/files/Pub32757.pdf. [Accessed: Jul. 29, 2025

[14] J. Phother-Simon, I. Hanif, T. Jonsson, and J. Liske, "High-Temperature corrosion of P91/T91, 304L, Sanicro 28 and Inconel 625 exposed at 600 °C under continuous KCl deposition," *Fuel,* vol. 357, p. 130012, 2024/02/01/ 2024, doi: https://doi.org/10.1016/j.fuel.2023.130012.

[15] H. Lindmark, T. Jonsson, and J. Liske, "A time-resolved study of PbCl2-induced corrosion of low-alloyed steel in the presence of water vapour at 400 °C," *Corrosion Science,* vol. 229, p. 111843, 2024/04/01/ 2024, doi: https://doi.org/10.1016/j.corsci.2024.111843.